Preparation of porous silica materials using a eucalyptus template method and its efficient adsorption of methylene blue

Wenxin Zhu
Nanning Normal University
Leping Liu (130078@nnnu.edu.cn)
Nanning Normal University
YuanXia Lao
Nanning Normal University
Yan He
Guangxi University

Research Article

Keywords: Quartz powder, Eucalyptus, Adsorption, Organic dye

Posted Date: April 26th, 2023

DOI: https://doi.org/10.21203/rs.3.rs-2844761/v1

Abstract

Mesoporous silica has become one of the primary adsorbent materials for solving dye wastewater pollution due to its high specific surface area and good adsorption properties. However, the high cost of the traditional chemical synthesis method limits its wide application. In this thesis, low-cost and high-efficiency porous silica adsorbent materials (PSAM) were successfully prepared by dissolving quartz powder in NaOH solution and depositing and growing in the pores of eucalyptus wood under hydrothermal conditions using eucalyptus wood as a templating agent. The experimental results showed the prepared materials have a loose, porous slit pore structure and many active adsorption sites. The adsorption efficiency of methylene blue was high, reaching more than 85% within 10 min, and the maximum adsorption amount was 90.01 mg/g. The adsorption process was by the pseudo-first-order pseudo-second-order, and Langmuir models. The analysis of thermodynamic data showed that the adsorption of methylene blue by PSAM was a heat-absorbing process and spontaneous. Therefore, PSAM can be effectively used for the application of methylene blue dye removal in water.

1. Introduction

Water is a vital material resource for human health and development. Water pollution from industrial production is an increasingly severe threat to freshwater resources, causing toxic damage to plants, animals, and humans. Industrial organic dyes are one of the leading causes of surface and groundwater pollution. Organic dyes typically have complex structures and are not readily biodegradable. Most contain elements such as nitrogen and sulfur, which are highly toxic and carcinogenic [1, 2]. One such dye is methylene blue (MB). This cationic thiazine dye can remain in aquatic systems long if left untreated, endangering marine organisms' survival and destroying the ecosystem's balance [3]. Industrial wastewater must be effectively treated before discharge to reduce pollution of inflowing water sources. Current methods for treating industrial wastewater and organic dyes can be classified into physical, biological, and chemical treatments. Commonly used methods include electrochemical degradation, photocatalytic degradation, Fenton oxidation, adsorption, and biological anaerobic degradation [4–6]. Each method has its advantages and disadvantages. The adsorption method has received extensive research attention owing to its low cost, convenience, low energy consumption, and low temperature and pressure requirements [7].

In recent years, the commonly used adsorbents for treating organic dyes in wastewater by adsorption include commercial activated carbon, but commercial activated carbon has a high cost, which limits its application [8]. So other materials have better research and application in adsorption, such as biomass carbon materials and nano metal oxides, which are widely used in dye adsorption and degradation. Biomass carbon materials (e.g., lychee shell, sugarcane peel, wood chips, etc.) and nano oxides (e.g., TiO_2, ZnO, SiO_2, etc.) possess the advantages of large specific surface area and pores, which make them excellent adsorbent materials. [9–13].

Mesoporous silica is usually prepared using the sol-gel method with surfactants as soft templating agents; the high preparation cost limits its large-scale application. Karine et al. [14] prepared mesostructured silica materials via a synergistic self-assembly and liquid crystal templating mechanism using polyoxyethylene fluoroalkyl ether and quaternary ammonium surfactants as substrates. Su et al. [15] used ZnO nanorod arrays as macroporous templates and CTAB as a mesoporous template to synthesize graded mesoporous silica films. However, most surfactants are petrochemicals, which are costly and do not meet the requirements of a low-carbon environment. Current applications of mesoporous silica include the adsorption of heavy metal ions and organic pollutants. Zhang et al. [16] used an improved oil–water biphasic layered coating to synthesize silica with a fibrous structure. The resulting particles were modified with CPBA and studied as cis-diol adsorbents for adsorption performance. The simple, green, and efficient preparation of mesoporous silica materials with good adsorption properties is still a problem worthy of further investigation.

Eucalyptus is the world's most widely distributed hardwood tree and a relatively abundant timber resource in Guangxi [17]. Due to its low cost and abundance, it is commonly used in papermaking and building materials for home use and as a carbon source for fuel and other materials [18–20]. Eucalyptus wood has many pore structures, and some lignin is dissolved under robust alkaline solutions. The pore size increases, providing a suitable environment for SiO_2 deposition. Quartz has the most stable and abundant crystal structure of SiO_2. Quartz powder can be quickly dissolved in a NaOH solution in a hydrothermal environment at a specific temperature and pressure.

This paper aims to obtain a low-cost and efficient mesoporous silica adsorbent material using eucalyptus wood as a templating agent. Under hydrothermal conditions, quartz powder is rapidly dissolved in NaOH solution and deposited and grown in the pores of eucalyptus wood after calcination to remove the templating agent. Moreover, the prepared mesoporous silica material showed highly efficient adsorption performance for methylene blue dye in water. In addition, the lignin-containing waste solution and the precipitated SiO_2 can be recycled as a bio-binder after concentration. For example, Juan et al. [21] prepared high-density fiberboard (HDF) from wheat straw under alkaline conditions using lignin as a natural adhesive, Yang et al. [22] first Lignin was catalyzed by sodium hydroxide and phenolized by phenol at high temperature. Lignin was washed by ether and precipitated by acid to prepare phenolic resin by replacing part of the phenol with this product. In the present study, a report on preparing mesoporous silica using eucalyptus wood as a template has yet to be prepared. This thesis focuses on the structure of PSAM and its adsorption performance and adsorption mechanism on methylene blue dye to provide a new idea for preparing and applying efficient dye adsorbents.

2. Materials And Methods

2.1. materials

The quartz powder in this experiment was purchased from Chengde Group Company in Beihai, Guangxi, and the eucalyptus wood was from Chongzuo City, Guangxi. Sodium hydroxide is an analytically pure

reagent purchased from Chongqing Chuandong Chemical Group Co. Methylene blue is also an analytically pure reagent, purchased from Tianjin Zhiyuan Chemical Reagent Co. Deionized water was homemade in the laboratory and used for the preparation of chemical solutions. The XRD spectrum of raw quartz powder is shown in Fig. 1.

2.2 Synthesis of PSAM

Sodium hydroxide (30 g) and quartz powder (15 g) with a mass ratio of 2:1 were mixed and stirred well, and the concentrations of sodium hydroxide were 2 mol/L (2M), 4 mol/L (4M), 6 mol/L (6M) and 8 mol/L (8M), respectively. After the hydrothermal treatment, the waste solution and precipitate were concentrated and recovered for the bioadhesive. The eucalyptus slices were sonicated for 5 min in an ultrasonic cleaner with an operating frequency of 37 kHz three times. 80°C oven drying and calcination at 600°C for 2 h. The calcined material was ground to obtain a black powder and collected for subsequent testing.

2.3 Characterization

The crystal structures of the prepared samples were characterized using X-ray diffraction (XRD, Rigaku MiniFlex 600 diffractometer, Japan) with Cu Kα radiation at a scanning rate of 5°/min at a voltage of 40 kV and a current of 15 mA at 5–80°. The structure of the substances was analyzed by recording Fourier transform infrared spectrograms (FTIR, Thermo Scientific Nicolet IS50, USA) using the KBr particle method. Scanning electron microscopy (SEM) images of the studied catalysts were acquired on a field emission scanning electron microscope (FE-SEM, Hitachi SU8220, Japan) device. The specific surface area and the prepared samples' pores were tested by adsorption and desorption in N_2 with a surface area porosity analyzer (BET, Micromeritics ASAP2460, USA). The samples were degassed at 300°C for 6 h before measurement. The zeta potential measurements were carried out using a nanoparticle analyzer (Horiba, SZ-100, Japan).

2.4 Adsorption performance

The adsorption kinetics were performed at room temperature (20 ± 2°C) in the dark. Adsorbent (50 mg) was added to 50 mL of a 20 mg/L MB solution. The supernatant was shaken at 230 rpm and filtered through a needle filter (4 mL) at predetermined time intervals before measurement with a double-beam UV spectrophotometer at a wavelength of 664 nm.

The adsorption isotherms were also obtained at room temperature (20 ± 2°C) in the dark. Adsorption equilibrium was reached by adding 50 mg of adsorbent to 50 mL of MB solution at different concentrations (20–60 mg) and shaking at 230 rpm for 24 h. The supernatant (4 mL) was filtered and measured at 664 nm using a double-beam UV-Vis spectrophotometer (Shimadzu UV2600, Japan). Isothermal adsorption curves were fitted from Langmuir (5) and Freundlich (6) models.

The thermodynamics of attachment was measured at 20°C, 30°C, and 40°C by adding 50 mg of adsorbent to a solution of MB at a concentration of 20 mg/L. After shaking at 230 rpm for 24 h, 4 mL of the supernatant was filtered, and the absorbance was measured at a wavelength of 664 nm using a dual-

beam UV-Vis spectrophotometer (Shimadzu UV2600, Japan). The thermodynamic parameters were obtained by fitting Eqs. (8), (9), and (10).

The adsorbent's effect on MB solution's adsorption was investigated at different temperatures (20–60°C) and pH (pH = 2–8).

2.4 Related formulas

The adsorption amount (q_t, mg/g) and equilibrium adsorption capacity (q_e, mg/g) of MB for the samples at different adsorption times (t) are expressed as

$$q_t = \frac{(C_0\text{-}C_t)\ V}{m} \quad (1)$$

$$q_e = \frac{(C_0\text{-}C_e)\ V}{m} \quad (2)$$

where C_0 is the starting concentration of the adsorbent solution (MB solution) (mg/L); C_t is the concentration of the adsorbent (MB solution) at a particular moment t (mg/L); C_e is the concentration of the adsorbent (MB solution) at the moment of equilibrium (mg/L); V is the volume of the adsorbent solution (MB solution) (L), and W is the mass of the adsorbent (g).

· Adsorption kinetic

$q_t = q_e\ (1\text{-}e^{-k_1 t})$	**Pseudo-first order [23]**	**(3)**
$q_t = \frac{k_2 q_e^2 t}{1+k_2 q_e t}$	Pseudo-second order [24]	(4)

where k_1 is the adsorption rate constant (min^{-1}) for the pseudo-first-order model; k_2 is the adsorption rate constant (g/mg/min) for the pseudo-second-order model, and q_e and q_t are the MB uptakes (mg/g) at equilibrium and at time t (min), respectively.

·Adsorption isotherm

$\log q_e = \log K_F + \frac{1}{n}\log C_e$	Freundlich [25]	(5)
$\frac{C_e}{q_e} = \frac{1}{K_L q_m} + \frac{C_e}{q_m}$	Langmuir [26]	(6)
$R_L = \frac{1}{1+R_L+C_0}$		(7)

where K_L (L/mg) and K_F [(mg/g)/(mg/L)n] represent the Langmuir and Freundlich adsorption coefficients, respectively; n is the exponential coefficient, and R_L (L/mg) is the Langmuir constant.

·Adsorption thermodynamics [13]

$K_L = m \frac{q_e}{C_e}$	(8)
$\Delta G = -RT\ln K_L$	(9)
$\ln K_L = \frac{\Delta S}{R} - \frac{\Delta H}{RT}$	(10)

where K_L is the partition coefficient, ΔS (J/K mol) is the standard entropy change; ΔH (kJ/mol) is the standard enthalpy; ΔG (kJ/mol) is the standard free energy change; R is the ideal gas constant (8.314 J/mol/ K), and T is the temperature (K).

3. Results And Discussion

3.1. Characterization

3.1.1 XRD

Figure 2 shows the XRD patterns of specimens hydrothermally heated at 120°C for 24 h with different NaOH solution and quartz powder concentrations. Peaks at 2θ = 20.86°, 26.64°, and 50.05° were observed for all specimens with complete coincidence with the characteristic peaks of quartz crystals (PDF#89-1961), corresponding to crystallographic planes (100), (011), and (112). As the NaOH concentration increased, the intensity of the characteristic peaks of the quartz crystals decreased. After the hydrothermal reaction, the surface of the quartz powder particles reacted with sodium hydroxide solution to form many silica hydroxyl groups. Quartz particles with silica hydroxyl groups on the surface were deposited in the pore structure of eucalyptus chips via a condensation reaction between them. The PSAM was obtained after calcination to remove the template. With an increase in the NaOH solution concentration, many non-bridging oxygen active sites were formed in the pore channels of PSAM to balance its charge with Na+. The calcined PSAM formed Na_2CO_3 crystals after the adsorption of CO_2

from the air. With NaOH concentrations of 2M and 4M, Na_2CO_3 crystals were not detected in the XRD spectra; the presence of Na_2CO_3 crystals was determined from later FTIR analysis. With NaOH concentrations of 6M and 8M, characteristic peaks of Na_2CO_3 were observed at 2θ = 20.06°, 34.19°, 35.16°, 37.93°, 39.85°, 40.99°, 46.28°, and 48.10° in the spectra of the PSAM specimens, in addition to the characteristic peaks of quartz crystals (PDF#72–0628).

3.1.2 FTIR

Figure 3 shows the FTIR spectra of wood specimens treated with different concentrations of NaOH solutions. The figure shows that all four materials correspond to the anti-integrated stretching vibration of H-O-H at 3440 cm^{-1} and the bending vibration peak of O-H at 1590 cm^{-1}. [27]. As can be seen from the figure, the characteristic peaks are weak mainly because the water is removed from PSAM after calcination at 600°C. The PSAM specimens correspond to the antisymmetric stretching vibration of Si-O-Si and the bending vibration of Si-O in quartz crystals at 1090 cm^{-1} and 461 cm^{-1}, respectively. The characteristic peaks of quartz crystals gradually weakened with increasing NaOH concentration, which is consistent with the trend of the characteristic peaks of quartz crystals in the XRD patterns. The specimens corresponded to the antisymmetric stretching vibration and symmetric stretching vibration of CO_3^{2-} at 1440 cm^{-1} and 877 cm^{-1} [28, 29]. Respectively, the peak of the stretching vibration of CO_3^{2-} gradually increased with increasing NaOH concentration, indicating that the Na_2CO_3 crystals gradually increased in PSAM, which is consistent with the XRD results.

3.1.3 SEM

Figure 4 shows SEM images of the materials treated with different NaOH concentrations after magnification at different multiples. It is observed in the figure that all four materials have a very loose internal structure with many widely spaced voids, providing more active sites for dye adsorption. The pore size of the PSAM decreased with increasing NaOH concentration. The NaOH solution had two leading roles in preparing the materials: (1) dissolving part of the lignin in the pore channels of eucalyptus chips and (2) reacting with the surface of quartz particles. The surface hydroxylated particles were condensed and deposited in the pore channels of eucalyptus chips. From the microstructural analysis, the second effect was dominant; the number of quartz particles deposited into the pore channels by dissolution–condensation increased with increasing NaOH concentration, and the pore size formed after calcination to remove the template were smaller. Analysis of XRD and FTIR data indicates the mechanism of action and microstructure change pattern of the NaOH solution during the preparation of the materials. However, all four materials generally had more pores and better adsorption performance for MB.

3.1.4 BET

Table 1
Surface area and pore characteristics of PSAM samples.

Samples	$S_{BET}(m^2/g)$	$V_{total}(cm^3/g)$	$D_{ave}(nm)$
2M	88.05	0.082	3.707
4M	69.17	0.065	3.786
6M	54.07	0.041	3.017
8M	61.75	0.041	2.645

Figure 5(a) shows the four materials' N_2 adsorption–desorption isotherms. According to the IUPAC classification, the prepared materials' N_2 adsorption–desorption isotherms are type II isotherms with an H3 lagging loop [12]. As observed in the figure, the relative pressure increased gently with increasing pressure between 0 and 0.8. When the relative pressure was more significant than 0.8, the adsorption increased rapidly with increasing pressure, mainly due to capillary condensation in the mesopores and macropores. Different types of hysteresis loops represent different types of pore structures. The H3 hysteresis loop in the figure indicates the presence of mesopores and large slit pores in the prepared material [30]. Figure 5(b) shows the pore size distribution of the four materials; the range of the pore centers of the four materials was between 3–4 nm, and the pore size was approximately 3.7 nm. Table 1 shows the four materials' specific surface area and pore size; the specific surface area, cumulative pore volume, and pore size showed an overall decreasing trend with increasing sodium hydroxide concentration. Formation of the pore size of PSAM is based on two factors: (1) the surface hydroxylation of quartz particles and the residual pores of the unfilled eucalyptus pore channels formed by the condensation reaction deposited in the pore channels of eucalyptus chips and the pores between the piles of particles, and (2) the slit pores left by the removal of the eucalyptus chip template. When the NaOH concentration is low, there are fewer hydroxyl groups on the surface of the quartz particles; the quartz deposited in the pore channels is not filled, and there are pores between the pile of particles. The eucalyptus pore channels dissolve less under the action of NaOH solution, and more slit holes remain after calcination. When the concentration of NaOH increased, the surface of the quartz particles dissolved and produced a large number of hydroxyl groups, and the amount deposited in the structure of eucalyptus pore channels through the condensation reaction increased. The accumulation between particles was denser, whereas the pore walls of the eucalyptus chips were thinner under the action of a high NaOH concentration. Smaller slit holes were formed after calcination. Overall, the specific surface areas and pore sizes of all four materials were not significantly different, and they showed good adsorption properties for MB. The variation pattern of the pore structure can be determined from microstructure analysis.

3.1.5 Zeta potential

Figure 6. As the pH of the solution increases from 2 to 10, the zeta potential of PSAM shows a decreasing trend, and the value changes from positive to negative. The data in the figure shows that the zero point charges (pH_{pzc}) of PSAM are 2.12, 2.09, 2.11, 2.12. Since MB is a cationic dye, when the pH of the solution is lower than the pH_{pzc} value ($pH < pH_{pzc}$), the surface of PSAM is positively charged, which is not favorable for the adsorption of MB; on the contrary, when the pH of the solution is higher than the pHpzc value ($pH > pH_{pzc}$), the surface of PSAM is negatively charged, which will be favorable for MB adsorption [31].

3.2. Adsorption of MB

Figure 7(a) shows the adsorption rates of different materials on MB. It can be observed from the figure that the adsorption rates of the four prepared materials on MB increased sharply in the first 10 min, and the adsorption amount could reach 17.64 mg/g in the 10th min. With the increase of time, the adsorption rates increased slowly and gradually stabilized to reach the equilibrium, and the adsorption amount at the equilibrium was 20 mg/g. When the NaOH concentration was 2 M and 4 M, the pore size of PSAM was more significant, and there were more slit pores in When methylene blue adsorption was carried out, more dyes entered the internal active site dyes through internal diffusion, in addition to those adsorbed on the surface of PSAM. When the concentration of sodium hydroxide is 6M and 8M, the pore size of PSAM is small, the slit pores are small, more active sites on the surface, and more dyes are adsorbed.

Meanwhile, due to the significant molecular weight of dyes, the spatial site resistance is considerable, and the amount of active sites entering inside and outside through internal diffusion is reduced. The total active adsorption sites of PSAM prepared from different NaOH solutions were consistent; therefore, the adsorption rates of methylene blue were the same. The trend analysis of PSAM adsorption rates was consistent with the previous XRD, FTIR, and SEM analysis that PSAM is a porous material with abundant active sites. The main reason for the different trends from the BET data is that the adsorption properties of the dye are related to the active adsorption sites in the pore channels and the active adsorption sites on the surface of the material. In this study, as the specific surface area and pore size decreased with the increase of sodium hydroxide concentration, the amount of dye entering the internal pore channels decreased due to the spatial location. However, the active adsorption sites on the material surface increased, so the total adsorption rate was unchanged. Figure 7(b) shows the effect of different temperatures on MB adsorption. With the increase in temperature, the adsorption rate of MB increased for the four materials. The adsorption process is heat absorption, and the temperature increase accelerates the binding rate of dye molecules and materials [32]. From the following thermodynamic analysis, this speculation can be proved. Figure 7(c) shows the effect of different pH on the adsorption of MB, from which it can be seen that the adsorption of MB was not satisfactory under highly acidic conditions (pH = 2). However, between pH 4–10, PSAM was suitable for the adsorption of MB on the four materials because the pH was higher than pH_{pzc}, which was favorable for adsorption, indicating that the material can be applied to the treatment of weakly acidic, neutral and alkaline dye wastewater, which is consistent with the previous zeta potential analysis.

3.2.1. Adsorption kinetics

Table 2
Kinetics parameters for MB Adsorption on PSAM samples.

Samples	pseudo-first-order			pseudo-second-order		
	q_e(mg g^{-1})	k_1(min^{-1})	R^2	q_e(mg/g)	k_2(mg^{-1} g^{-1} L^{-1})	R^2
2M	19.77	0.83	0.998	19.88	0.32	0.998
4M	20.06	0.67	0.995	20.26	0.15	0.997
6M	19.49	0.71	0.994	19.66	0.18	0.996
8M	18.93	0.43	0.986	19.34	0.06	0.995

Figure 8 shows a fit to the adsorption kinetics of PSAM on MB, where (a) is a pseudo-first-order kinetic model and (b) is a pseudo-second-order kinetic model. Table 2 presents the parameters of the kinetic fits for the four materials. The kinetic fit curves show that the adsorption of MB by the materials increased gradually with time, with a faster increase in the first 10 min, followed by a flattening until equilibrium. This is because the material provided more adsorption sites at the beginning of the adsorption process. However, with increasing time, the adsorption sites on the material were occupied by dye molecules. With an increase in adsorption time, the dye concentration decreased; the adsorption efficiency decreased, and the adsorption reached saturation [11]. The fitted data show that the R^2 values of the pseudo-first-order and pseudo-second-order kinetic models are close to 1; thus, both models apply to the adsorption of MB by PSAM [33, 34]. In a previous study, the same adsorption kinetic trends were observed for the synthesis of nano-silica-coated magnetic carbonaceous adsorbents for the adsorption of MB in water using a low-temperature hydrothermal carbonization technique (HCT), indicating that the adsorption of MB by PSAM is controlled by multiple processes and not by a single process [13, 35].

3.2.2. Adsorption isotherms

Table 3
Adsorption isotherm parameters for MB Adsorption on PSAM samples.

Samples	Langmuir				Freundlich		
	q_m (mg g^{-1})	K_L (L mg^{-1})	R_L (L mg^{-1})	R^2	n	K_F (L $mg^{-1})^{1/n}$(mg g^{-1})	R^2
2M	90.01	1.56	0.03	0.981	1.74	55.74	0.946
4M	80.97	1.02	0.05	0.990	1.92	38.57	0.988
6M	64.52	0.49	0.09	0.983	2.48	23.19	0.977
8M	61.16	1.01	0.05	0.978	2.85	29.40	0.917

Table 4
Comparison of the adsorption capacity of MB by different adsorbents

Adsorbent	q_m(mg/g)	Reference
Acrylated composite hydrogel (ACH)	56.61	[36]
Activated lignin-chitosan extruded pellets (ALiCE)	36.25	[4]
Carboxymethyl chitosan-modified magnetic-cored dendrimers (CCMDs)	96.31	[37]
Mesoporous silicon carbon (MSC)	156.56	[38]
Magnetic starch-based composite hydrogel microspheres (SCHMs)	88.33	[39]
Hydrophobic (surface modified) silica aerogel (MSA)	65.74	[40]
Paintosorp	44.64	[41]
Sago-grafted silica 80:20	10.31	[42]
PSAM	90.01	This work

Figure 9 shows the results of the PSAM fit to the MB adsorption isotherm, where Fig. (a) and Fig. (b) are the Langmuir model fit curves, and Fig. (c) is the Freundlich model fit curve. Table 3 shows the parameters of the adsorption isotherm fit. From the data of the graphs, it can be seen that the R^2 of the Langmuir model is close to 1, so the Langmuir model is more applicable to the adsorption of PSAM on MB [43]. The Langmuir model applies to the adsorption of the monomolecular layer, so the adsorption of PSAM on MB is of monomolecular layer adsorption. From the data in Table 3, the maximum adsorption amounts of the four materials are not significantly different. However, in comparison, the adsorption amount of 2M PSAM reaches 90.01 mg/g, the most considerable adsorption amount among the four

materials, consistent with the previous BET data. K_L denotes the Langmuir constant, which indicates the affinity of the adsorbate for the binding site. The separation factor R_L can be calculated by Eq. (7) when $0 < R_L < 1$ favors the adsorption, as observed from the Langmuir fit data, so all four materials prepared are favorable for MB adsorption [44]. Moreover, the fitted data from the Freundlich model also reveals that the n values of all four materials are between 1 and 10, n is a parameter describing the adsorption strength, and when $1 \leq n \leq 10$, the adsorption is favored, so all the four prepared PSAMs show good adsorption on MB [34, 45]. Meanwhile, the maximum adsorption of different adsorbents on MB dyes is listed in Table 4, which shows that PSAM can effectively remove organic dyes from water.

3.2.3. Adsorption thermodynamics

Table 5
Various thermodynamics parameters for the Adsorption of MB onto 2M PSAM.

Samples	ΔG^0(kJ mol^{-1})	ΔH^0(kJ mol^{-1})	ΔS^0(kJ mol^{-1} K^{-1})	R^2
2M	-1.128	21.364	76.765	0.946

Adsorption thermodynamics is an essential basis for studying whether adsorption occurs spontaneously. Figure 10 shows the lnKL-1/T curve for 2M PSAM; the relevant thermodynamic parameters can be calculated from the curves in the figure, as shown in Table 5. From the data in the table, $\Delta H > 0$ indicates that the adsorption of PSAM on MB is heat-absorbing. If the temperature of the reaction is increased, the adsorption rate of PSAM on MB can be enhanced, which is consistent with the effect of temperature on PSAM adsorption. Based on a value of ΔH between 0 kJ mol-1 and 84 kJ mol-1, it can be judged that the adsorption is mainly a physical adsorption process [46]. A positive value of ΔS indicates that the adsorption process is disorderly, increasing at the solid–liquid interface. The value of ΔG is less than 0, indicating that the adsorption of MB by PSAM is spontaneous [47, 48].

3.3. Adsorption mechanism of MB on PSAM

The adsorption effect of adsorbents on adsorbates is not only determined by the physical structure and chemical properties of the adsorbent material itself, such as the specific surface area and pore size of the material but also by other influences, such as the interaction between the adsorbent and the adsorbate and the charge on the adsorbent surface [13]. When adsorption occurs, the adsorbent and adsorbent are bound in different ways, usually through ion exchange, hydrogen bonding, electrostatic interactions, dipole-dipole interactions, hydrophobic interactions, and surface metal cation coordination between adsorbent and adsorbent. Figure 11 shows the FTIR spectra of 2M PSAM before and after the adsorption of MB. It can be observed that the peaks at 1440 cm^{-1} and 877 cm^{-1} disappear before and after the adsorption, and the peaks at these two locations are the characteristic peaks of CO_3^{2-}, thus indicating that MB^+ can be adsorbed with CO_3^{2-} by electrostatic gravitation. At the same time, the characteristic peaks of SiO_2 also changed slightly, indicating that the material's structure did not change before and

after adsorption, but MB^+ could also bind to SiO_2 by electrostatic interaction [13, 49]. Therefore, the dye molecules are adsorbed on the surface of PSAM by electrostatic interaction. Moreover, PSAM can also bind to the N atom in MB by hydrogen bonding [3, 13]. The adsorption mechanism of MB is shown in Scheme 1. Moreover, the added wood is structurally increasing the specific surface area of the material and providing more dye adsorption sites for the material itself.

4. Conclusion

This study successfully prepared a low-cost and high-efficiency porous silica adsorbent material via a hydrothermal synthesis method using quartz powder as the raw material and eucalyptus wood chips as the template with the template different concentrations of sodium hydroxide. The prepared material was used for the adsorption of MB; the experimental results are presented as follows:

1. Sodium hydroxide reacted with the surface of quartz particles. Hydroxylated quartz particles were deposited in the pore channels of eucalyptus wood chips through a condensation reaction, and pore channels were formed between the stacked quartz particles. After removing the template, sodium hydroxide dissolved part of the lignin in the pore channels and formed slit pores.
2. As the concentration of NaOH increased, the characteristic peaks of quartz crystals of PSAM weakened; the number of active sites formed on the surface increased, and the internal pore size decreased.
3. Adsorption of MB by the four PSAMs was divided into surface and intra-pore adsorption. The pore sizes of the PSAM materials prepared with 2M and 4M sodium hydroxide were larger, indicating mainly intra-pore adsorption. The pore sizes of the PSAM materials prepared with 6M and 8M sodium hydroxide were smaller. Diffusion of MB into the pores was reduced owing to the spatial site resistance, indicating mainly surface adsorption. An adsorption rate of 85% was achieved in 10 min for the four PSAM materials, all of which showed good adsorption performance and rate.
4. The adsorption kinetics and isotherms were fitted for the four materials. The fitted data shows that they all fit the pseudo-first-order kinetic, pseudo-second-order kinetic, and Langmuir models, which indicates that a single process controls the adsorption of MB by PSAM and that the adsorption is a single molecular layer adsorption. Thermodynamic data show that the adsorption of MB by PSAM is a spontaneous heat-absorbing process. PSAM has potential applications due to its low preparation cost, wide availability of raw materials, and high efficiency in the adsorption of MB from wastewater.

Environmental Implications

A new porous silica adsorbent material was synthesized and tested for its adsorption performance on methylene blue using eucalyptus wood as a template as a simulated pollutant for industrial wastewater. The tests showed that the porous material has high adsorption efficiency for methylene blue in water and can reach more than 85% adsorption rate in ten minutes. Moreover, the adsorption process is spontaneous. The material can effectively remove toxic organic dyes in water.

Declarations

CRediT authorship contribution statement

Wenxin Zhu: Conceptualization, Methodology, Software, Validation, Investigation, Data curation, Writing - original draft; **Leping Liu**: Conceptualization, Supervision, Writing - review & editing; **YuanXia Lao**: Investigation, Writing - review & editing. **Yan He**: Conceptualization, Supervision, Writing - review & editing.

Declaration of Competing Interest

The authors declare that they have no known competing financial interests or personal relationships that could have appeared to influence the work reported in this paper.

Data availability

Data will be made available on request.

Acknowledgments

This work was supported by the National Natural Science Foundation of China (51962024).

References

1. X. Liu, J. Tian, Y. Li, et al., Enhanced dyes adsorption from wastewater via Fe3O4 nanoparticles functionalized activated carbon. Journal of Hazardous Materials. 373, 397-407, (2019). https://doi.org/https://doi.org/10.1016/j.jhazmat.2019.03.103.
2. Y. Yu, N. Qiao, D. Wang, et al., Fluffy honeycomb-like activated carbon from popcorn with high surface area and well-developed porosity for ultra-high efficiency adsorption of organic dyes. Bioresource Technology. 285, 121340, (2019). https://doi.org/https://doi.org/10.1016/j.biortech.2019.121340.
3. C. Djilani, R. Zaghdoudi, F. Djazi, et al., Adsorption of dyes on activated carbon prepared from apricot stones and commercial activated carbon. Journal of the Taiwan Institute of Chemical Engineers. 53, 112-121, (2015). https://doi.org/https://doi.org/10.1016/j.jtice.2015.02.025.
4. A. B. Albadarin, M. N. Collins, M. Naushad, et al., Activated lignin-chitosan extruded blends for efficient adsorption of methylene blue. Chemical Engineering Journal. 307, 264-272, (2017). https://doi.org/https://doi.org/10.1016/j.cej.2016.08.089.
5. S. Mahalingam, J. Ramasamy and Y.-H. Ahn, Enhanced Photocatalytic Degradation of Synthetic Dyes and Industrial Dye Wastewater by Hydrothermally Synthesized G–CuO–Co3O4 Hybrid

Nanocomposites Under Visible Light Irradiation. Journal of Cluster Science. 29(2), 235-250, (2018). https://doi.org/10.1007/s10876-017-1329-3.

6. T. Ochiai, Y. Iizuka, K. Nakata, et al., Efficient electrochemical decomposition of perfluorocarboxylic acids by the use of a boron-doped diamond electrode. Diamond and Related Materials. 20(2), 64-67, (2011). https://doi.org/https://doi.org/10.1016/j.diamond.2010.12.008.
7. W. Xiang, X. Zhang, J. Chen, et al., Biochar technology in wastewater treatment: A critical review. Chemosphere. 252, 126539, (2020). https://doi.org/https://doi.org/10.1016/j.chemosphere.2020.126539.
8. M. Rafatullah, O. Sulaiman, R. Hashim, et al., Adsorption of methylene blue on low-cost adsorbents: A review. Journal of Hazardous Materials. 177(1), 70-80, (2010). https://doi.org/https://doi.org/10.1016/j.jhazmat.2009.12.047.
9. L. G. da Silva, R. Ruggiero, P. d. M. Gontijo, et al., Adsorption of Brilliant Red 2BE dye from water solutions by a chemically modified sugarcane bagasse lignin. Chemical Engineering Journal. 168(2), 620-628, (2011). https://doi.org/https://doi.org/10.1016/j.cej.2011.01.040.
10. V. S. Mane and P. V. Vijay Babu, Kinetic and equilibrium studies on the removal of Congo red from aqueous solution using Eucalyptus wood (Eucalyptus globulus) saw dust. Journal of the Taiwan Institute of Chemical Engineers. 44(1), 81-88, (2013). https://doi.org/https://doi.org/10.1016/j.jtice.2012.09.013.
11. H. Mittal and S. S. Ray, A study on the adsorption of methylene blue onto gum ghatti/TiO2 nanoparticles-based hydrogel nanocomposite. International Journal of Biological Macromolecules. 88, 66-80, (2016). https://doi.org/10.1016/j.ijbiomac.2016.03.032.
12. H. Mittal, S. M. Alhassan and S. S. Ray, Efficient organic dye removal from wastewater by magnetic carbonaceous adsorbent prepared from corn starch. Journal of Environmental Chemical Engineering. 6(6), 7119-7131, (2018). https://doi.org/https://doi.org/10.1016/j.jece.2018.11.010.
13. H. Mittal, R. Babu, A. A. Dabbawala, et al., Low-Temperature Synthesis of Magnetic Carbonaceous Materials Coated with Nanosilica for Rapid Adsorption of Methylene Blue. ACS Omega. 5(11), 6100-6112, (2020). https://doi.org/10.1021/acsomega.0c00093.
14. K. Assaker, M.-J. Stebe and J.-L. Blin, Mesoporous Mesoporous silica materials from diluted and concentrated solutions of nonionic fluorinated and ionic hydrogenated surfactants mixtures. Colloids and Surfaces a-Physicochemical and Engineering Aspects. 536, 242-250, (2018). https://doi.org/10.1016/j.colsurfa.2017.02.056.
15. X. Su, J. Tao, S. Chen, et al., Uniform hierarchical silica film with perpendicular macroporous channels and accessible ordered mesopores for biomolecule separation. Chinese Chemical Letters. 30(5), 1089-1092, (2019). https://doi.org/10.1016/j.cclet.2019.01.022.
16. W. Zhang, S. Li, J. Zhang, et al., Synthesis and adsorption behavior study of magnetic fibrous mesoporous silica. Microporous and Mesoporous Materials. 282, 15-21, (2019). https://doi.org/10.1016/j.micromeso.2019.03.022.

17. S. Suganya and P. S. Kumar, Evaluation of environmental aspects of brew waste-based carbon production and its disposal scenario. JOURNAL OF CLEANER PRODUCTION. 202, 244-252, (2018). https://doi.org/10.1016/j.jclepro.2018.08.143.
18. K. Elyounssi, F. X. Collard, J. A. N. Mateke, et al., Improvement of charcoal yield by two-step pyrolysis on eucalyptus wood: A thermogravimetric study. FUEL. 96(1), 161-167, (2012). https://doi.org/10.1016/j.fuel.2012.01.030.
19. G. Kumar, S. Shobana, W.-H. Chen, et al., A review of thermochemical conversion of microalgal biomass for biofuels: chemistry and processes. Green Chemistry. 19(1), 44-67, (2017). https://doi.org/10.1039/C6GC01937D.
20. M. E. Vallejos, J. Kruyeniski and M. C. Area, Second-generation bioethanol from industrial wood waste of South American species. Biofuel Research Journal. 4(3), 654-667, (2017). https://doi.org/10.18331/BRJ2017.4.3.4.
21. J. Dominguez-Robles, Q. Tarres, M. Delgado-Aguilar, et al., Approaching a new generation of fiberboards taking advantage of self lignin as green adhesive. International Journal of Biological Macromolecules. 108, 927-935, (2018). https://doi.org/10.1016/j.ijbiomac.2017.11.005.
22. S. Yang, J.-L. Wen, T.-Q. Yuan, et al., Characterization and phenolation of biorefinery technical lignins for lignin-phenol-formaldehyde resin adhesive synthesis. Rsc Advances. 4(101), 57996-58004, (2014). https://doi.org/10.1039/c4ra09595b.
23. S. K. Lagergren, About the theory of so-called Adsorption of soluble substances. Kungliga Svenka. Vetenspsakademiens Handlingar. 24, 1-39, (1898). https://doi.org/.
24. Y. S. Ho and G. McKay, Sorption of dye from aqueous solution by peat. Chemical Engineering Journal. 70(2), 115-124, (1998). https://doi.org/https://doi.org/10.1016/S0923-0467(98)00076-1.
25. H. Freundlich, Über die adsorption in L¨osungen. Ztschrift Phys. Chemistry. 57(1), 385–470, (1907). https://doi.org/.
26. I. Langmuir, THE ADSORPTION OF GASES ON PLANE SURFACES OF GLASS, MICA AND PLATINUM. Journal of the American Chemical Society. 40(9), 1361-1403, (1918). https://doi.org/10.1021/ja02242a004.
27. X. Sun, L. Yang, T. Dong, et al., Removal of Cr(VI) from aqueous solution using amino-modified Fe3O4-SiO2-chitosan magnetic microspheres with high acid resistance and adsorption capacity. Journal of Applied Polymer Science. 133(10), (2016). https://doi.org/10.1002/app.43078.
28. P. Yu, R. J. Kirkpatrick, B. Poe, et al., Structure of calcium silicate hydrate (C-S-H): Near-, mid-, and far-infrared spectroscopy. Journal of the American Ceramic Society. 82(3), 742-748, (1999). https://doi.org/.
29. M. A. Trezza and A. E. Lavat, Analysis of the system 3CaO·Al2O3–CaSO4·2H2O–CaCO3–H2O by FT-IR spectroscopy. Cement and Concrete Research. 31(6), 869-872, (2001). https://doi.org/https://doi.org/10.1016/S0008-8846(01)00502-6.
30. M. Thommes, K. Kaneko, A. V. Neimark, et al., Physisorption of gases, with special reference to the evaluation of surface area and pore size distribution (IUPAC Technical Report). Pure and Applied

Chemistry. 87(9-10), 1051-1069, (2015). https://doi.org/10.1515/pac-2014-1117.

31. C. Ni, J. Wang, Y. Guan, et al., Self-powered peroxi-coagulation for the efficient removal of p-arsanilic acid: pH-dependent shift in the contributions of peroxidation and electrocoagulation. Chemical Engineering Journal. 391, 123495, (2020). https://doi.org/https://doi.org/10.1016/j.cej.2019.123495.
32. N. Hassan, A. Shahat, I. M. El-Deen, et al., Synthesis and characterization of NH2-MIL-88(Fe) for efficient adsorption of dyes. Journal of Molecular Structure. 1258, (2022). https://doi.org/10.1016/j.molstruc.2022.132662.
33. Y. S. Ho and G. McKay, A Comparison of Chemisorption Kinetic Models Applied to Pollutant Removal on Various Sorbents. Process Safety and Environmental Protection. 76(4), 332-340, (1998). https://doi.org/https://doi.org/10.1205/095758298529696.
34. T. A. Khan, S. Dahiya and I. Ali, Use of kaolinite as adsorbent: Equilibrium, dynamics and thermodynamic studies on the adsorption of Rhodamine B from aqueous solution. Applied Clay Science. 69, 58-66, (2012). https://doi.org/10.1016/j.clay.2012.09.001.
35. Y. Li, A. R. Zimmerman, F. He, et al., Solvent-free synthesis of magnetic biochar and activated carbon through ball-mill extrusion with Fe3O4 nanoparticles for enhancing adsorption of methylene blue. Science of the Total Environment. 722, (2020). https://doi.org/10.1016/j.scitotenv.2020.137972.
36. J. Wang, X. Meng, Z. Yuan, et al., Acrylated Composite Hydrogel Preparation and Adsorption Kinetics of Methylene Blue. Molecules. 22(11), 1824, (2017). https://doi.org/https://doi.org/10.3390/molecules22111824.
37. H.-R. Kim, J.-W. Jang and J.-W. Park, Carboxymethyl chitosan-modified magnetic-cored dendrimer as an amphoteric adsorbent. Journal of Hazardous Materials. 317, 608-616, (2016). https://doi.org/https://doi.org/10.1016/j.jhazmat.2016.06.025.
38. S. Zhang, Y. Gao, H. Dan, et al., Effect of washing conditions on adsorptive properties of mesoporous silica carbon composites by in-situ carbothermal treatment. Science of The Total Environment. 716, 136770, (2020). https://doi.org/https://doi.org/10.1016/j.scitotenv.2020.136770.
39. W. Li, H. Wei, Y. Liu, et al., Fabrication of novel starch-based composite hydrogel microspheres combining Diels-Alder reaction with spray drying for MB adsorption. Journal of Environmental Chemical Engineering. 9(5), 105929, (2021). https://doi.org/https://doi.org/10.1016/j.jece.2021.105929.
40. H. Han, W. Wei, Z. Jiang, et al., Removal of cationic dyes from aqueous solution by adsorption onto hydrophobic/hydrophilic silica aerogel. Colloids and Surfaces A: Physicochemical and Engineering Aspects. 509, 539-549, (2016). https://doi.org/https://doi.org/10.1016/j.colsurfa.2016.09.056.
41. Momina, S. Mohammad and I. Suzylawati, Study of the adsorption/desorption of MB dye solution using bentonite adsorbent coating. Journal of Water Process Engineering. 34, 101155, (2020). https://doi.org/https://doi.org/10.1016/j.jwpe.2020.101155.
42. Y. Rajan, Z. Ngaini and R. Wahi, Novel adsorbent from sago-grafted silica for removal of methylene blue. International Journal of Environmental Science and Technology. 16(8), 4531-4542, (2019). https://doi.org/10.1007/s13762-018-2043-x.

43. K. Y. Foo and B. H. Hameed, Insights into the modeling of adsorption isotherm systems. Chemical Engineering Journal. 156(1), 2-10, (2010). https://doi.org/10.1016/j.cej.2009.09.013.
44. Q. Wang, Z. Lai, C. Luo, et al., Honeycomb-like activated carbon with microporous nanosheets structure prepared from waste biomass cork for highly efficient dye wastewater treatment. Journal of Hazardous Materials. 416, (2021). https://doi.org/10.1016/j.jhazmat.2021.125896.
45. H. Mittal, V. Kumar, Saruchi, et al., Adsorption of methyl violet from aqueous solution using gum xanthan/Fe304 based nanocomposite hydrogel. International Journal of Biological Macromolecules. 89, 1-11, (2016). https://doi.org/10.1016/j.ijbiomac.2016.04.050.
46. H. Li, F. Zheng, J. Wang, et al., Facile preparation of zeolite-activated carbon composite from coal gangue with enhanced adsorption performance. Chemical Engineering Journal. 390, (2020). https://doi.org/10.1016/j.cej.2020.124513.
47. L. Hu, Z. Yang, L. Cui, et al., Fabrication of hyperbranched polyamine functionalized graphene for high-efficiency removal of Pb(II) and methylene blue. Chemical Engineering Journal. 287, 545-556, (2016). https://doi.org/10.1016/j.cej.2015.11.059.
48. A. Nasrullah, B. Saad, A. H. Bhat, et al., Mangosteen peel waste as a sustainable precursor for high surface area mesoporous activated carbon: Characterization and application for methylene blue removal. Journal of Cleaner Production. 211, 1190-1200, (2019). https://doi.org/10.1016/j.jclepro.2018.11.094.
49. M. Liu, L.-a. Hou, B. Xi, et al., Synthesis, characterization, and mercury adsorption properties of hybrid mesoporous aluminosilicate sieve prepared with fly ash. Applied Surface Science. 273, 706-716, (2013). https://doi.org/10.1016/j.apsusc.2013.02.116.

Scheme

Scheme 1 is available in the Supplementary Files section.

Figures

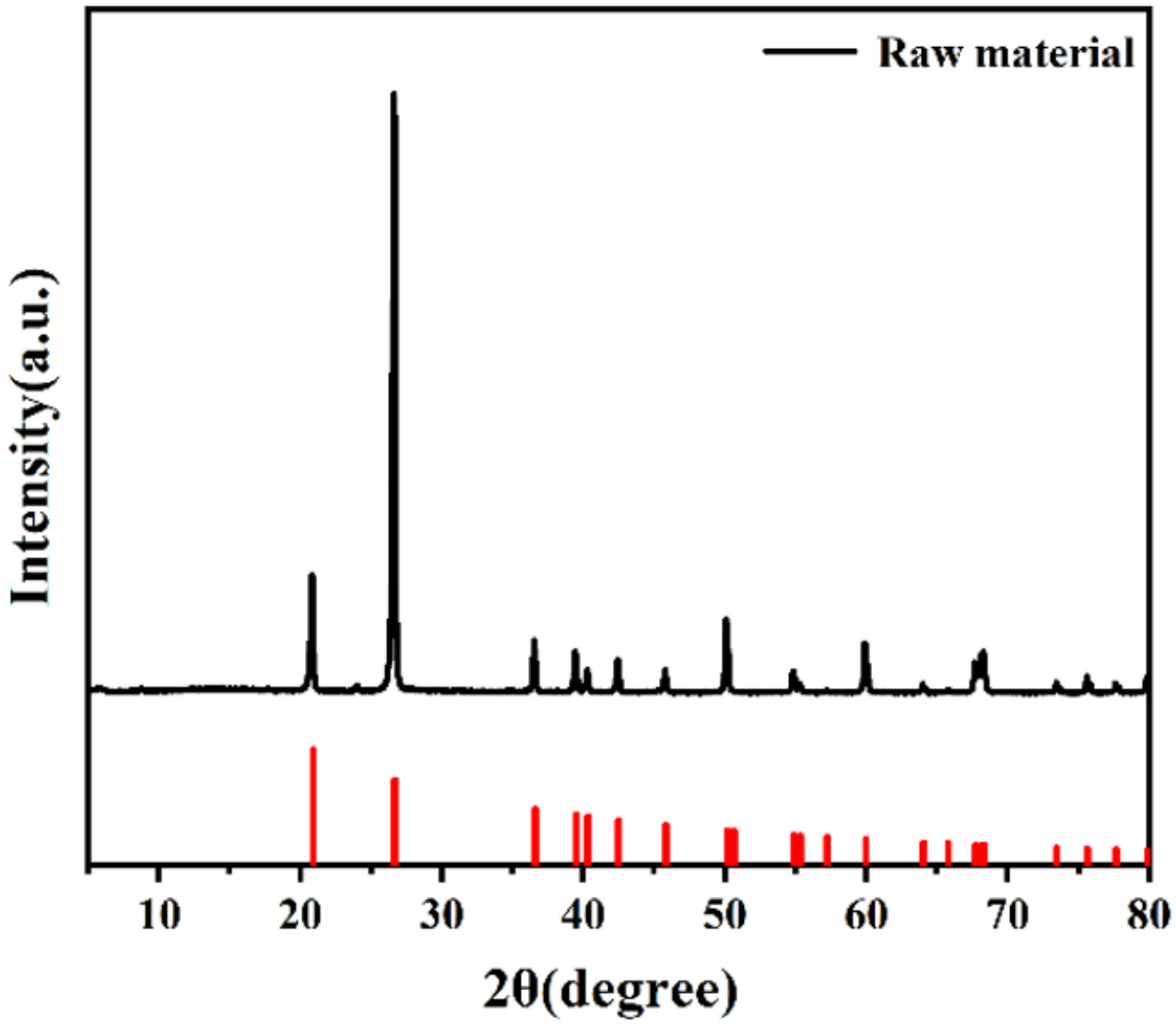

Figure 1

XRD patterns of the raw material and standard card of SiO_2 (PDF#89-1961).

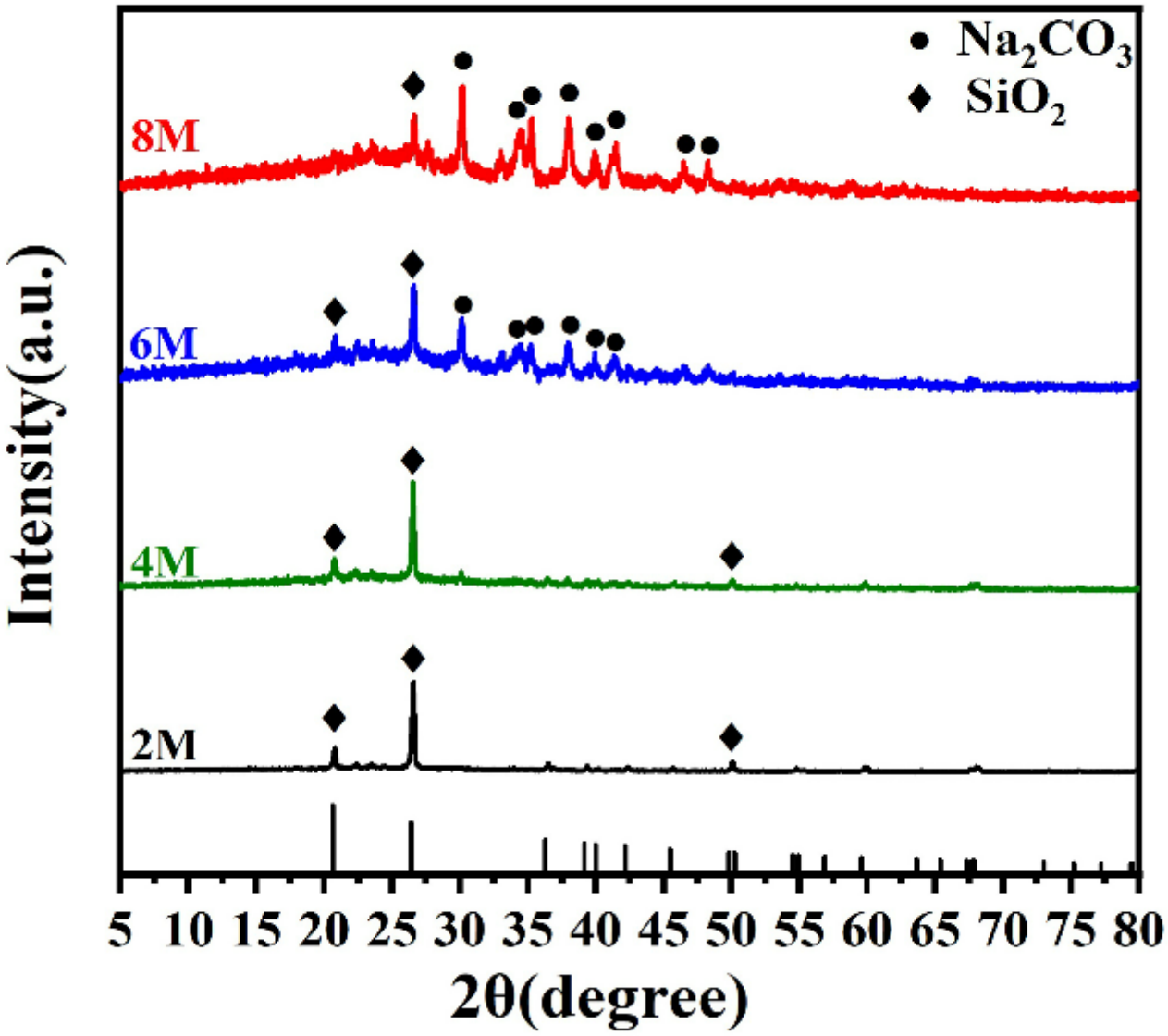

Figure 2

XRD patterns of PSAM prepared with different NaOH concentrations and standard card for SiO_2 (PDF#89-1961).

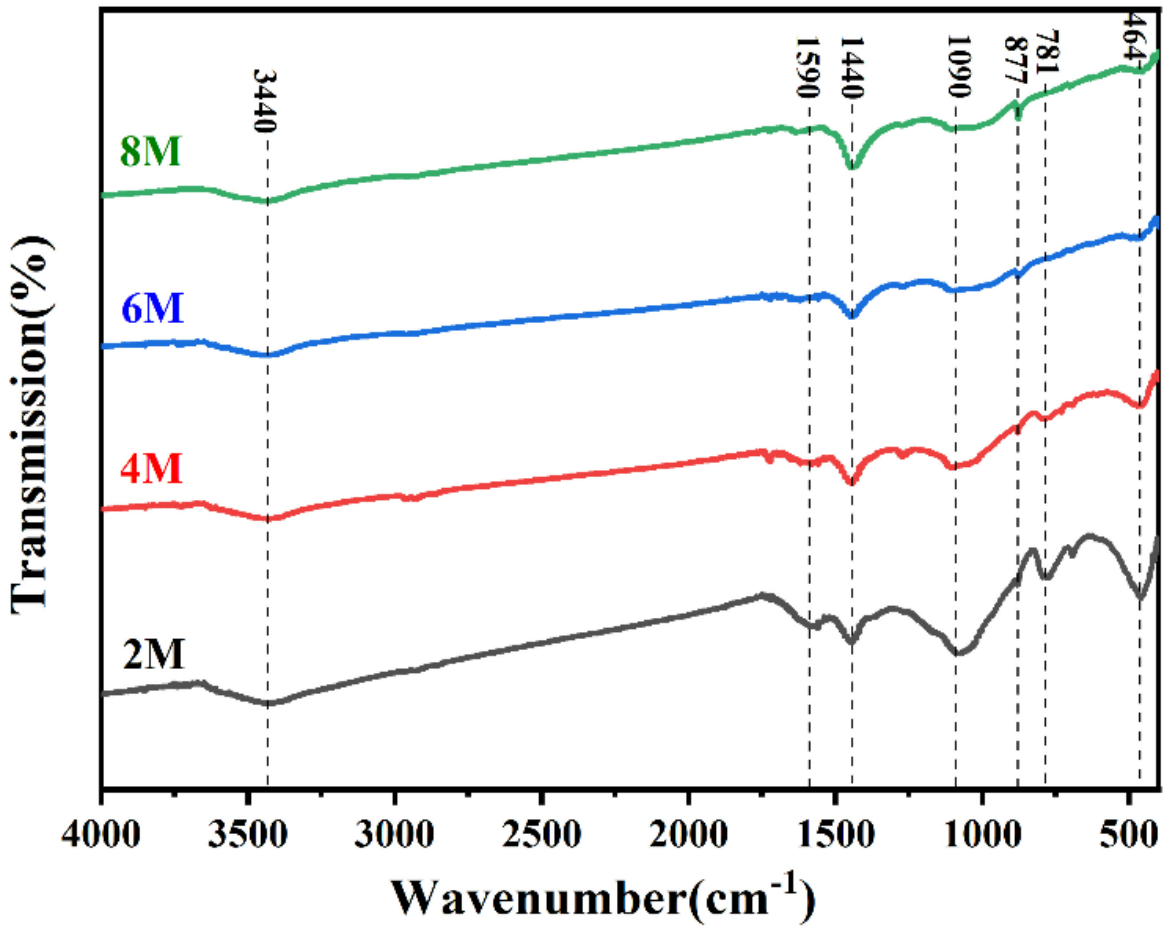

Figure 3

FTIR patterns of PSAM prepared with different NaOH concentration conditions.

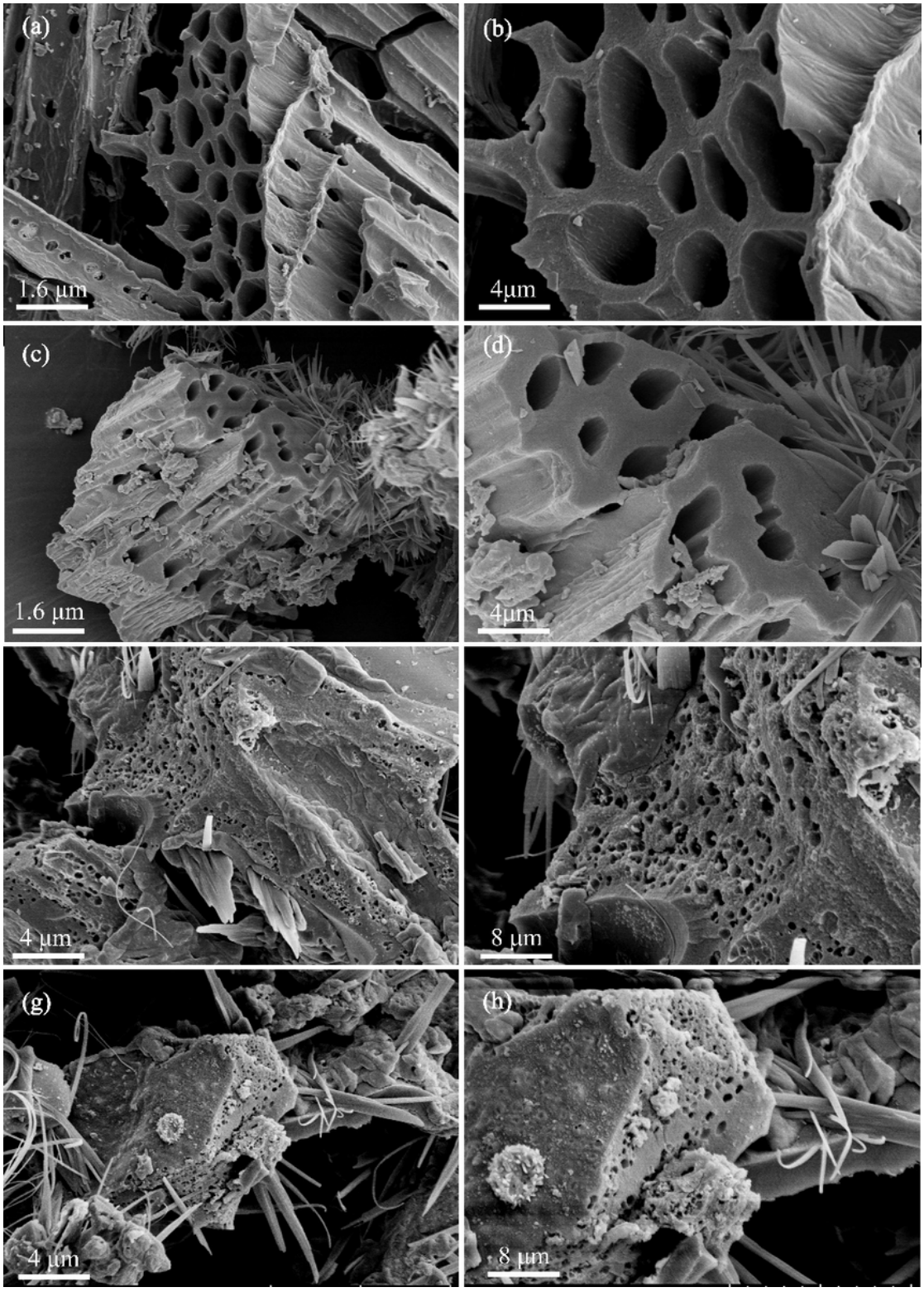

Figure 4

SEM images of PSAM prepared with different NaOH concentration conditions.

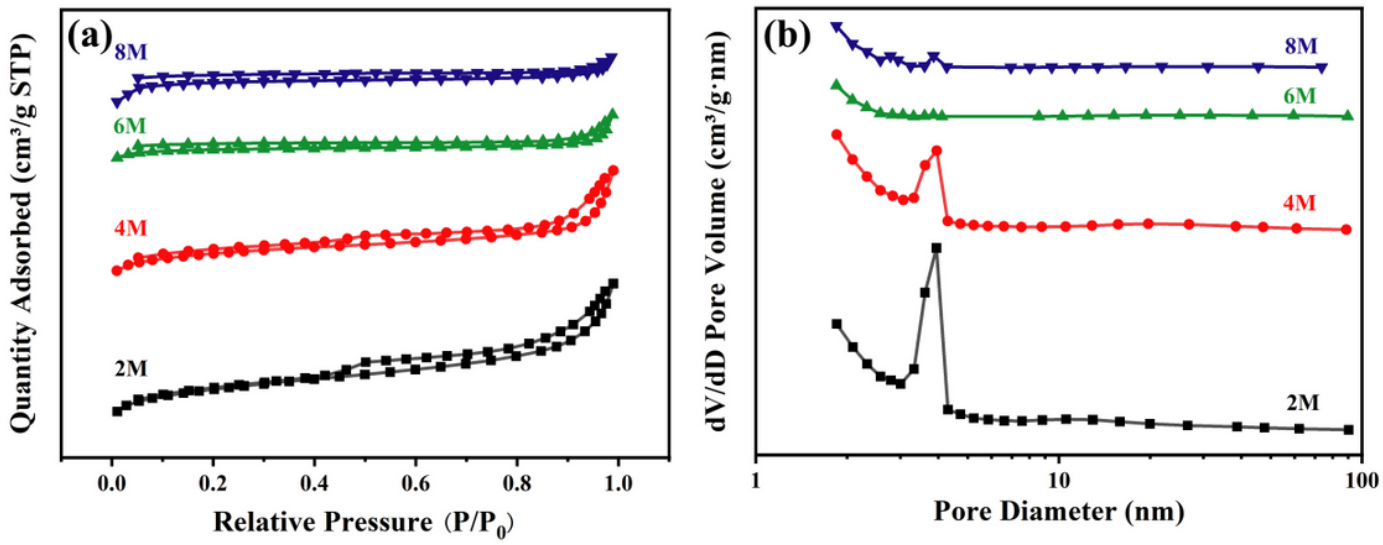

Figure 5

N_2 adsorption-desorption isotherms (a), pore-size distribution (b).

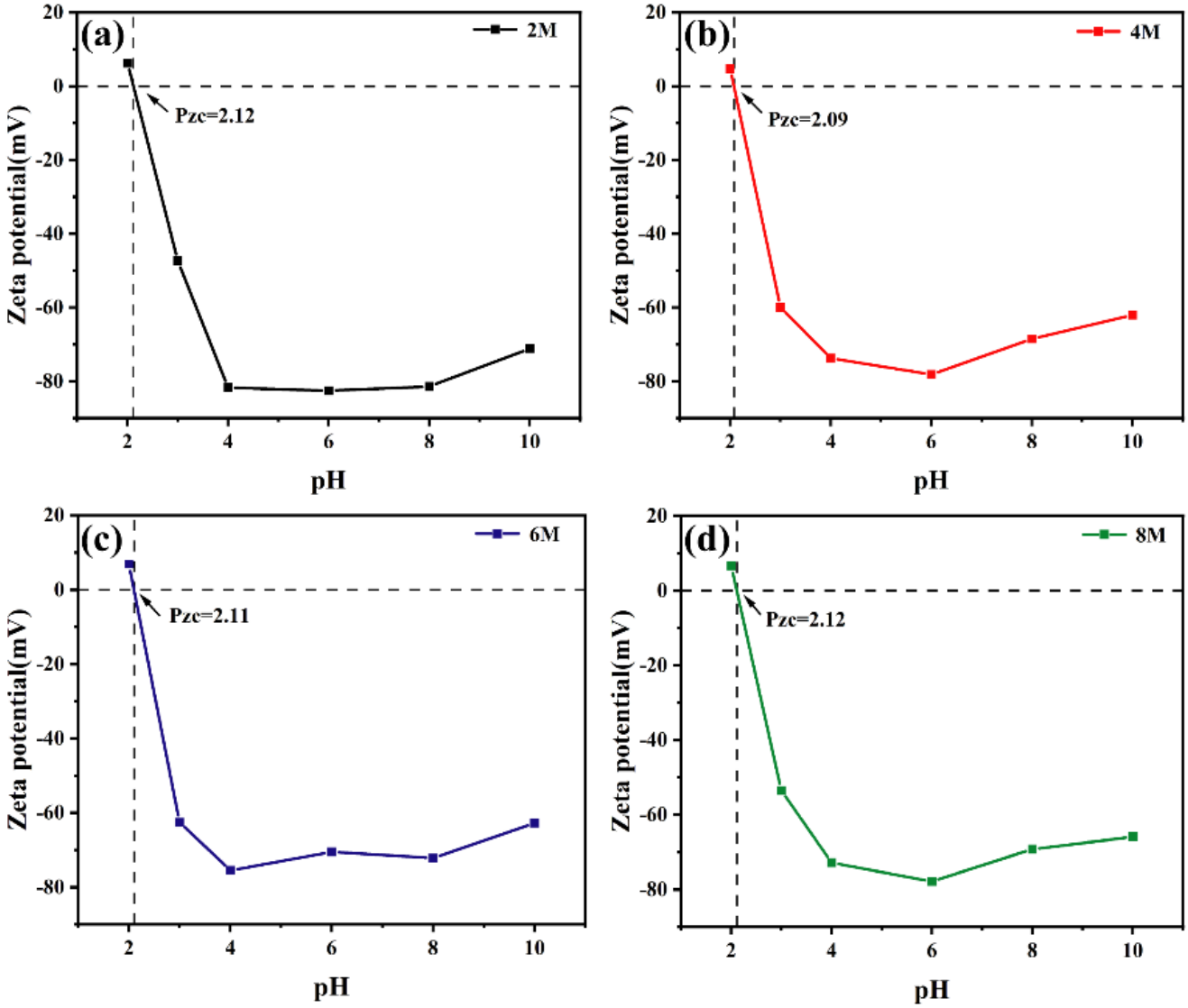

Figure 6

Zeta potential of 2M PSAM (a) 4M PSAM (b) 6M PSAM (c) 8M PSAM (d).

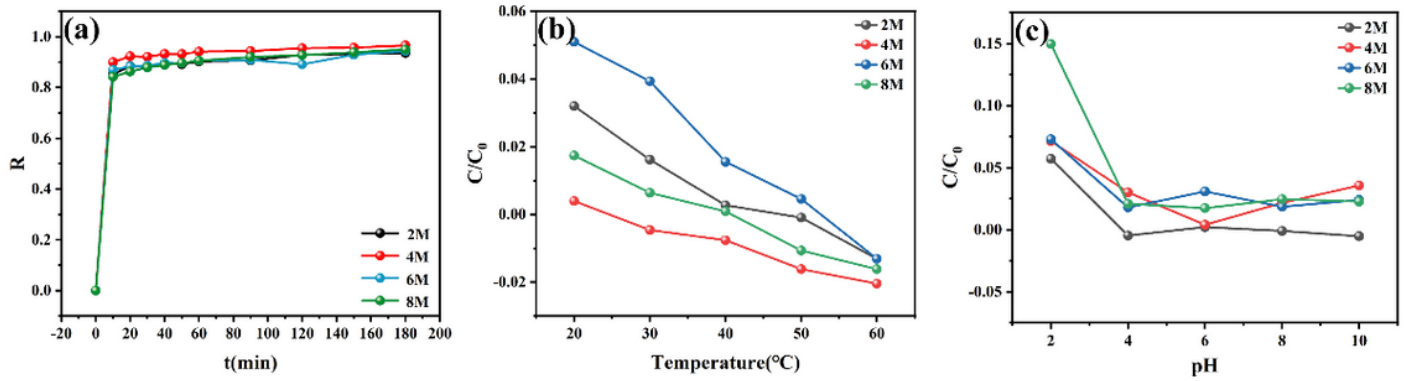

Figure 7

Effects of different samples (a) experiment temperature (b) and solution pH (c) on adsorption efficiency with MB (adsorbent dose, 50 mg; the volume of the medium, 50 mL; initial concentration, 20 mg/L; contact time, 24 h and temperature, 20°C).

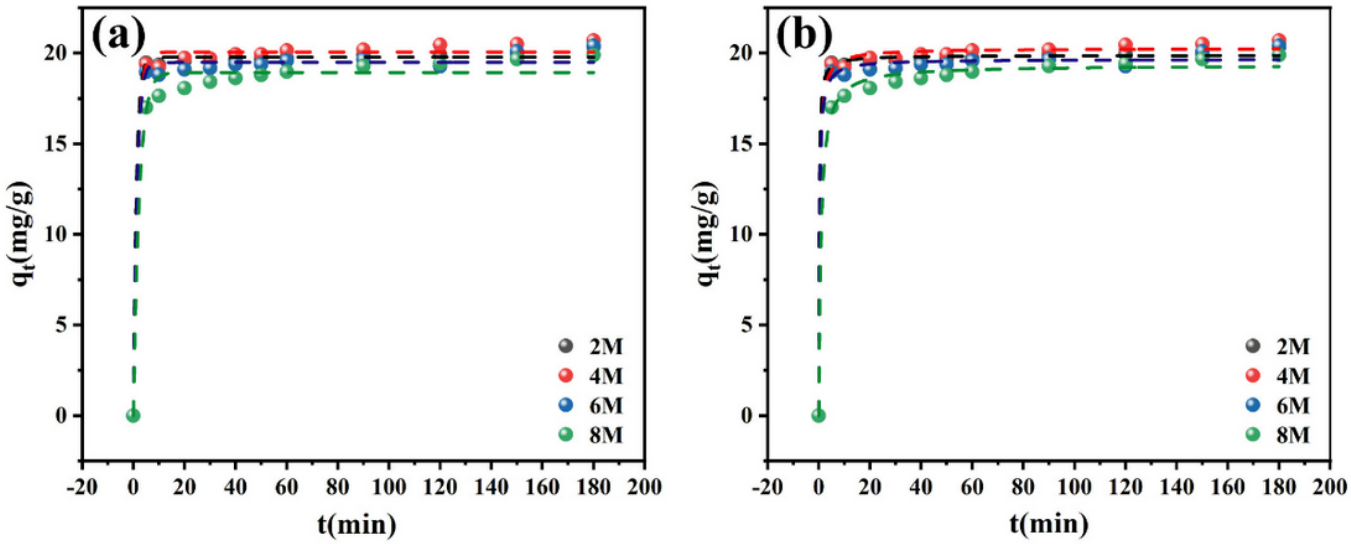

Figure 8

Adsorption kinetics of MB on PSAM samples:

pseudo-first-order (a); pseudo-second-order (b) (adsorbent dose, 50 mg; volume of the medium, 50 mL; initial concentration, 20 mg/L; pH, 6 and temperature, 20°C).

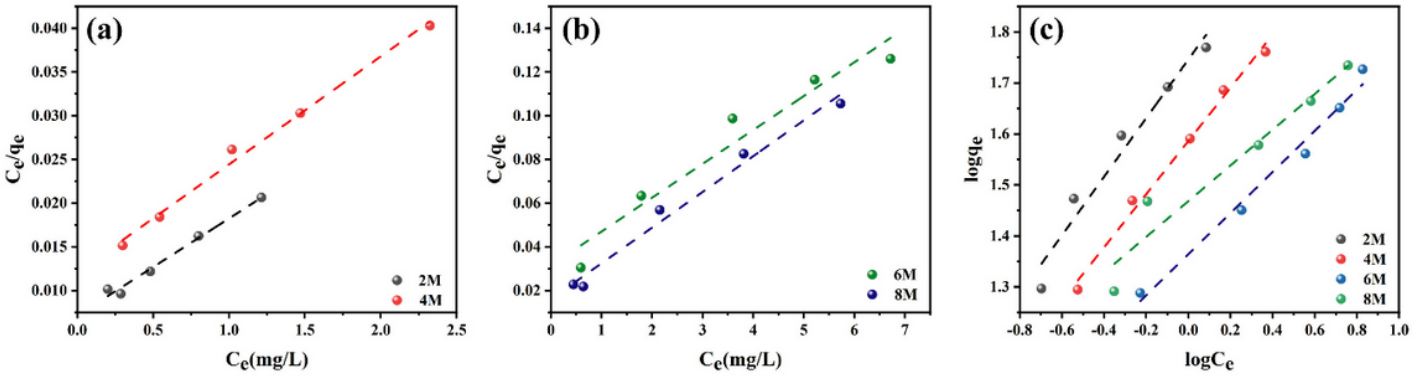

Figure 9

Adsorption isotherm of MB on PSAM samples: Langmuir (a, b); Freundlich (c) (adsorbent dose, 50 mg; the volume of the medium, 50 mL; initial concentration, 20-60 mg/L; pH, 6; contact time, 24 h and temperature, 20°C).

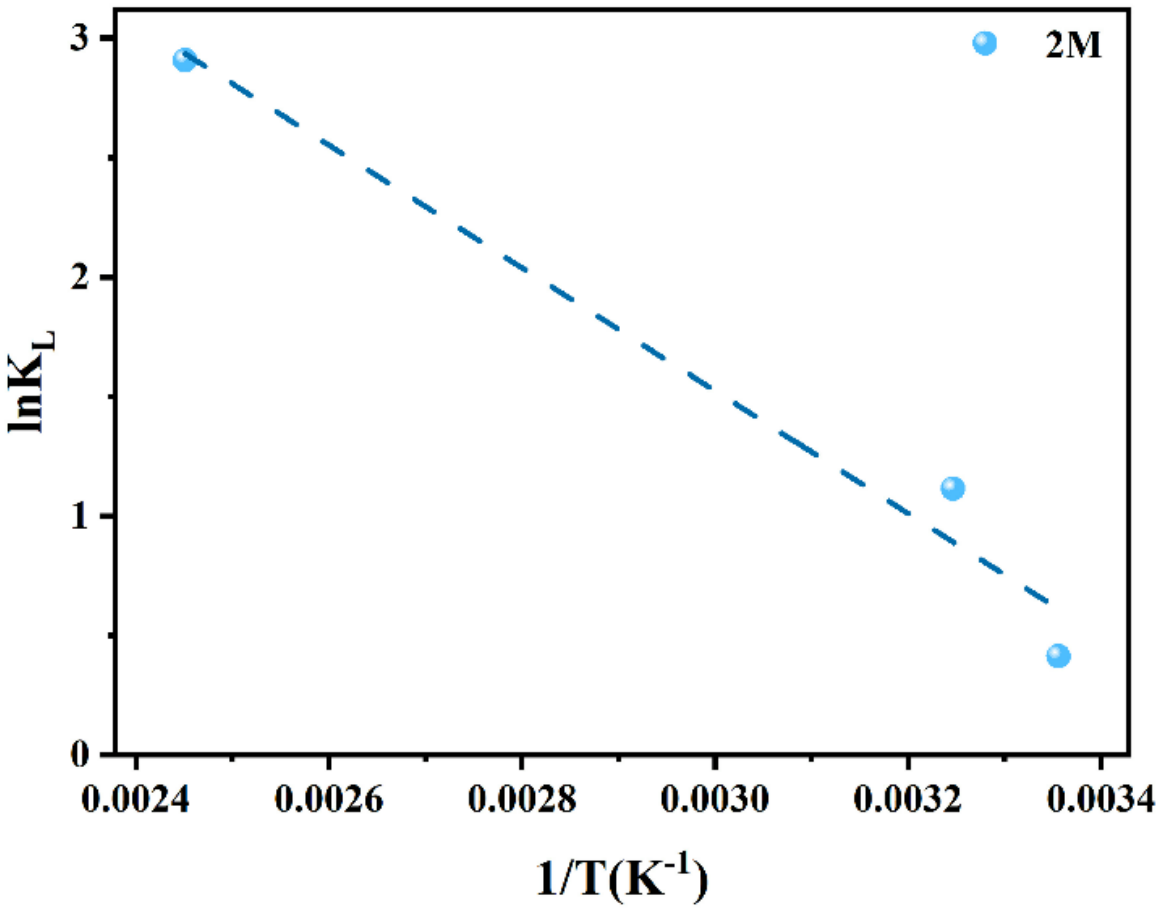

Figure 10

Vant's Hoffplot for the determination of different thermodynamics parameters for the Adsorption of MB onto 2M PSAM (adsorbent dose, 50 mg; the volume of the medium, 50 mL; initial concentration, 20 mg/L; pH, 6; contact time, 24 h and temperature, 20-40°C).

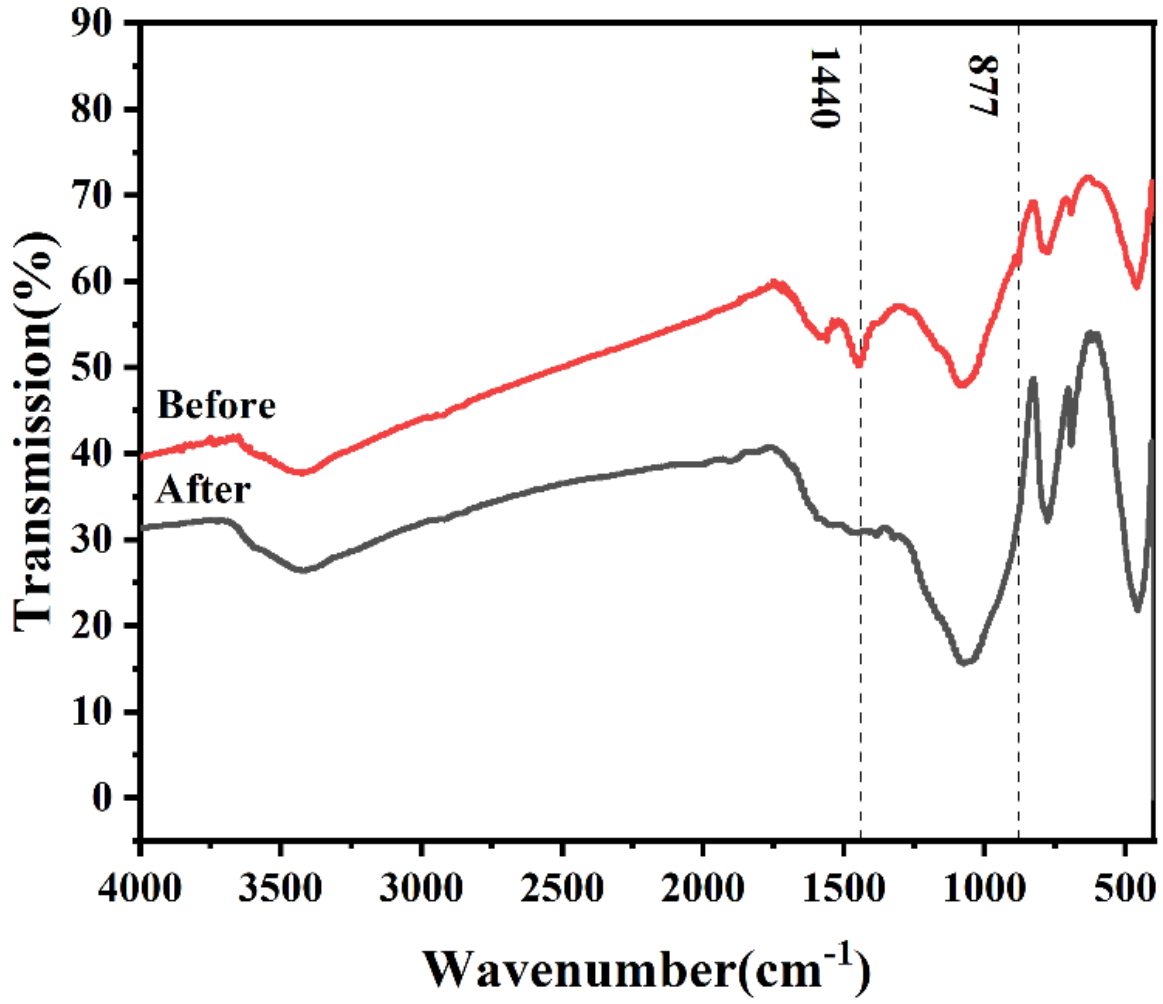

Figure 11

FTIR patterns before and after adsorption of 2M PSAM on MB.

Supplementary Files

This is a list of supplementary files associated with this preprint. Click to download.

- floatimage1.png
- floatimage13.png